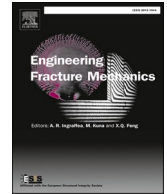




ELSEVIER

Contents lists available at ScienceDirect

Engineering Fracture Mechanics

journal homepage: www.elsevier.com/locate/engfracmech

Numerical study of mechanical properties and microcrack evolution of double-layer composite rock specimens with fissures under uniaxial compression

Qing Ma^{a,b}, Xiaoli Liu^{a,*}, Yunliang Tan^b, Derek Elsworth^c, Junlong Shang^d,
Danqing Song^a, Xuesheng Liu^b, Fayuan Yan^a

^a State Key Laboratory of Hydrosience and Engineering, Tsinghua University, Beijing 100084, China

^b College of Energy and Mining Engineering, Shandong University of Science and Technology, Qingdao 266590, China

^c Department of Energy and Mineral Engineering, G3 Center and Energy Institute, The Pennsylvania State University, University Park, PA 16803, USA

^d James Watt School of Engineering, University of Glasgow, Glasgow G128QQ, UK

ARTICLE INFO

Keywords:

Layered rock mass
Composite samples
Pre-existing fissures
Uniaxial compression
Mechanical behaviour

ABSTRACT

Layered and heterogenous fissured rock masses are ubiquitous in nature. Fissures exert significant influence as release surfaces and nucleation sites for failure in layered rock masses. However, key mechanisms controlling microcrack initiation and extension in layered and heterogenous rock masses remain unclear. We complete a suite of numerical (granular mechanics) and complementary physical compression experiments on layered rocks containing fissures in different modalities where the overlying layer is both stronger and stiffer. We complete this to understand the impact of local specimen and system stiffness on ultimate strength and modes of failure (stability). We systematically examine the influence of fissure angles, lengths and positions on the mechanical response, including observations of microcrack evolution and tendency for instability (i.e. rock bursting), constrained by acoustic emission (AE). Peak strength and overall elastic moduli vary in a predictable and systematic manner. The strengths and stiffnesses of the double-layer composite specimens fall between those of the homogeneous weak and strong single layer specimens. The AE counts, micro crack growth and failure characteristics of the double-layer composite specimens are closely related to the fissure angles, lengths and positions. Whether the weak rock or the strong rock contains fissures, the rock burst tendency of the double-layer composite specimens decreases in varying degrees—defining the potential of pre-blasting/fracturing to soften the mass. Fissure angles and lengths do not have to be too large. Additionally, failure in the double-layer composite specimens results not only from crack propagation in the weak layer, but also failure of the entire specimen when the length of the fissure in the strong layer is sufficiently large. These observations provide a reference for stability evaluation and disaster mitigation of layered rock masses in engineering.

* Corresponding author.

E-mail address: xiaoli.liu@tsinghua.edu.cn (X. Liu).

<https://doi.org/10.1016/j.engfracmech.2023.109403>

Received 10 April 2023; Received in revised form 21 May 2023; Accepted 5 June 2023

Available online 22 June 2023

0013-7944/© 2023 Elsevier Ltd. All rights reserved.

1. Introduction

Layered rock masses and layered structures are ubiquitous in nature (Fig. 1). Different from a single lithologic unit, layered rock masses are intrinsically anisotropic in strength, deformation, crack evolution and failure modes [1–4]. Tectonically driven deformation over geological time generates cracks, cavities and other defects [5,6]. Failure often nucleates from individual fractures that eventually coalesce and result in macroscopic failure and potential instability of the entire system [7–9]. Therefore, understanding the mechanical behavior and failure mechanisms that evolve in layered rock masses containing fissures is a prerequisite to predicting dynamic failure in rock mass engineering.

Crack initiation, propagation and coalescence in brittle materials containing fissures is known to be a function of size, flaw angles, flaw lengths and loading rates [10–17]. Average peak strengths are strongly influenced by flaw geometry and increasing the flaw inclination angle relative to the maximum principal stress first decreases then increases the peak strength. The spatial arrangement [18] of parallel joints and orientation of flaws at defect angles α and ligament angles β [12,19] determine the failure modes. Observations of failure modes for two different types of flaws show that wing cracks starts at the defect tip, but move to the middle of the defect, but may completely disappear under higher confining pressure [20]. In addition, various laboratory monitoring methods have been developed to study fracturing in pre-flawed rock specimens. Traditional methods use resistance strain gauges, but more constrained measurements may be made through photoelasticity, optical diffraction pattern recognition, scanning electron microscopy, ultrasonic detection and via acoustic emission (AE) monitoring [13,14]. Many of these methods follow the formation and extension of surface cracks but AE monitors internal cracks in the process of rock deformation and failure in real time [15–17]. Synchronous AE monitoring is a common and effective method to evaluate the strength and cracking behavior of brittle flawed rocks under anisotropic stress conditions [21–23]. Coupling the analysis of AE with measured stress–strain characteristics enables the complete cracking process to be followed and sub-divided into multiple levels, with each stage corresponding to different AE characteristics [22]. This enables quantitative interpretation and comparison of acoustic mechanical properties among materials [23]. AE testing can adapt to various harsh conditions and is not limited by the shape of the specimen. Many fracture criteria have been proposed for rocks containing fractures. For example, the new fracture criterion proposed by improving the fracture deformation model through shear test; the F criterion [24]. Such research on the influence of cracks/flaws on the mechanical properties and crack evolution of rock or rock like material provides reference for the following work on the mechanical properties and crack evolution of double-layer composite rock specimens with fissures.

AE is widely used in monitoring the mechanics and failure characteristics of rock containing cracks/flaws/fissures. However, predictions of response require forward modeling using the principles synthesized from such observations and characterizations [25]. Discrete element methods (DEM) are a powerful method to explore the impacts of microstructure on failure characteristics – as no failure modes need be defined a priori [26,27]. DEM methods follow the microscopic processes of fracturing with acoustic events represented by individual bond breaking, enabling the evolution of shear and tension cracks to be accurately identified [28–30]. In the parallel bonding model of PFC2D, the development of each crack produces a composite AE pulse. Thus, the AE characteristics of a failing virtual sample may be recovered as an AE time history [30–32]. This time history may be used as a diagnostic signature of the mode of failure [10,26,27]. Composite or anisotropic rock layers in the same or different rocks may be arbitrarily accommodated in the DEM simulations [31,32]. Thus, granular mechanics simulations are used in this work to follow the progressive failure and AE time-histories of fractured rocks.

From the foregoing, it is apparent that significant progress has been made in understanding the effect of cracks/fissures/flaws on the mechanical evolution of flawed rocks [35–37]. However, controls on microcrack evolution and styles of resulting failure (stable versus unstable) in heterogeneous samples with preexisting fissures remain indeterminate. Prior studies have demonstrated that rock type has an influence on crack evolution and failure modes [11–13,16,17]. In this work we examine the role of strength/stiffness in numerical models of layered strata with a strong/stiff upper half and containing fissures. Specifically we examine the influence of fissure inclination (angles), lengths and positions on the stress–strain response, peak strength, peak strain, elastic moduli and AE counts. Finally, we classify the potential for dynamic instability (rock bursting) of double-layer composite rock specimens with different fissures through the rock burst energy index K_E .



Fig. 1. Layered rock masses and fabricated layered structures.

2. Numerical modeling

2.1. Particle flow discrete element method

We use granular mechanics models³⁸ to analyze the failure characteristics of layered rocks accommodating large deformation and evolving naturally from linear elasticity to failure. In these DEM models, particle–particle interaction follows Newton’s second law with deformability enforced at the particle-to-particle contacts and bonds. Bonding includes contact bonding and linear parallel bonding. Among them, the parallel bonding model (Linearbond) can transfer forces and moments between different entities, and can also resist shear and tension caused by external forces.

The bond contact force–displacement relationship in the Linearbond model is shown in Fig. 2 [38,39] where the force–displacement relationship depends on the contact stiffness and contact relative displacement.

It can be seen from Fig. 2 that the force–displacement relationship of the parallel bonding model depends on the contact stiffness and contact relative displacement. F_n is the normal contact force. g_s is the normal contact gap. k_n is the normal contact stiffness. A is the contact area. M_t is the contact torque. θ_t is the torsion angle of the contact surface. k_s is the tangential contact stiffness. J is the polar moment of inertia of the parallel bonding section. F_s is the tangential contact force. s is the tangential displacement. M_b is the contact bending moment. I is the moment of inertia. θ_b is the rotation angle of the bonded contact surface. After obtaining the contact force and contact moment (including bending moment and torque) of the bonding key, the maximum normal and tangential contact stress on the contact surface can be calculated according to the following expressions. The calculation expression is as follows (ITASCA, 1999; Potyondy et al., 2004).

$$\sigma = \frac{F_n}{A} + \beta \frac{M_b \bar{R}}{I} \tag{1}$$

$$\tau = \frac{F_s}{A} + \beta \frac{M_t \bar{R}}{J} \tag{2}$$

$$A = \pi \bar{R}^2; I = \frac{1}{4} \pi \bar{R}^4; J = \frac{1}{2} \pi \bar{R}^4 \tag{3}$$

σ and τ are the maximum normal and tangential contact stress on the contact surface, respectively. β is the torque distribution coefficient, the value range is 0 ~ 1. In the classic model, this parameter is not set, and the default is 1. \bar{R} is the average contact radius. When the normal stress reaches the normal bonding strength, the contact between the particles will fail under tension. When the tangential stress reaches the shear strength, contact shear will fail.

2.2. Parameter calibration

Equivalent properties of the granular assemblage are defined through the particle–particle contacts. We assume mesoscale parameters and select microscale-parameters by to fit this global response [38,39]. In this paper, appropriate mesoscale parameters are selected through standard uniaxial compression experiments on complete specimens in the laboratory and fit using the modeling parameters of Table 1.

The stress–strain curves and schematics of failure modes are obtained from parallel physical and numerical uniaxial compression experiments, as shown in Fig. 3. From Fig. 3, the numerical results are observed to be congruent with those of the laboratory experiments.

2.3. Numerical modeling of virtual compression experiments

We assemble a layered column that comprises a stronger/stiffer upper layer with a weaker/softer lower layer (Fig. 4). We use five combinations of the layered configuration (Fig. 4) in the calculations. The samples comprise either the (weaker) material [W] (Fig. 4 (a)), the stronger material [S] (Fig. 4(b)), the stronger layer overlaying the weaker layer with no flaw [SW] (Fig. 4(c)), or the stronger

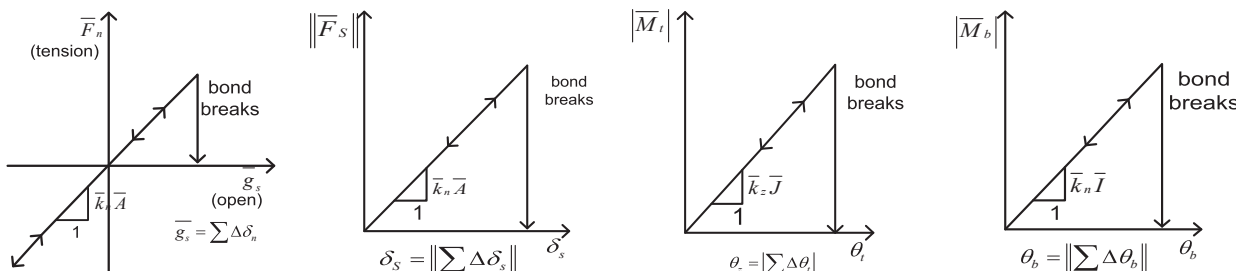


Fig. 2. Schematic diagram of contact force–displacement of Linearbond model [38,39].

Table 1
Microscale-mechanical parameters of lower and upper layers represented in the numerical simulations.

Contact parameter	Weak layer	Strong layer	Meaning
R_{min} (mm)	0.2	0.2	Minimum particle size
R_{max}/R_{min}	1.5	1.5	Ratio of maximum particle size to minimum particle size
E_c (GPa)	0.4	1.8	Effective modulus of particles
K_n/K_s	1.5	1.5	Ratio of the contact stiffness between the normal direction and the tangential bond of particles
\bar{E} (GPa)	0.6	2.4	Bond effective modulus
\bar{K}_n/\bar{K}_s	1.5	1.5	Ratio of normal to tangential bonding contact stiffness
σ_b (MPa)	8	16	Average and standard deviation of normal bond strength
c_b (MPa)	6	20	Mean and standard deviation of cohesive force
Φ ($^\circ$)	31	42	Bond internal friction angle
$\bar{\mu}$	0.5	0.5	Linear friction coefficient of particles

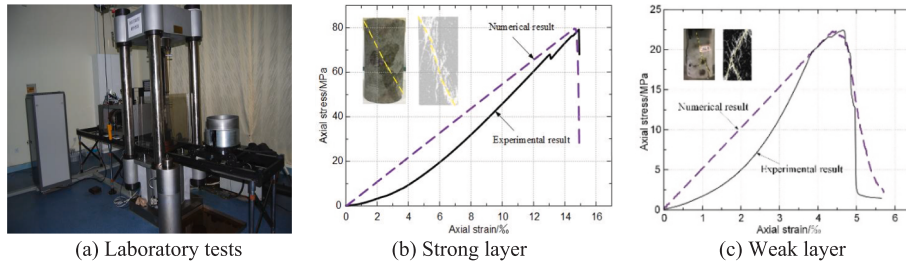


Fig. 3. Stress-strain curves obtained from laboratory and numerical experiments.

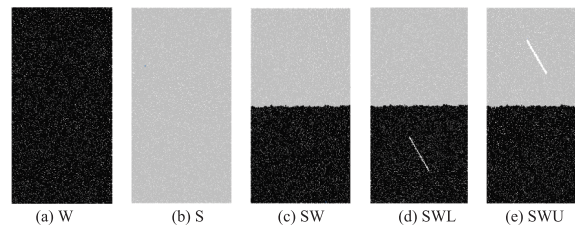


Fig. 4. Numerical models of weak [W](a), strong [S](b), strong overlaying weak either without a fracture [SW](c), or containing either a lower [SWL](d), or upper [SWU](e), fissure.

layer overlaying the weaker layer with a fissure in the lower layer [SWL] (Fig. 4(d)), or with a fissure in the upper layer [SWU] (Fig. 4(e)).

The numerical simulation of double-layer composite rock specimens under uniaxial compression is shown in Fig. 5. The loading rate is set as 0.05 mm/s to represent quasi-static loading. The servo mechanism in PFC is used to apply wall movement at constant velocity. Compressional loading is applied by keeping the lower wall static and applying a downward velocity of 0.05 mm/s to the upper wall with the overall stress-strain relationship, crack development, failure characteristics and energy accumulation to evaluate the propensity for bursting. This was repeated for all fracture inclination angles, lengths and positions.

3. Results and analysis

3.1. Stress-strain curves

A series of numerical (uniaxial) compression tests are completed on geometries W, SWL, SWU, SW and S, and the stress-strain curves and equivalent mechanical parameters obtained, as shown in Fig. 6 and Table 2. Peak strengths (from highest to lowest) are in the order $S > W > SWU > SW > SWL$, with peak strains as $W > S > SWU > SW > SWL$ and elastic moduli as $S > SW > SWU > SWL > W$. The relationship between the elastic moduli and rock type can be described by a nonlinear relationship $y = 2147.5662 - 2145.9546 / (1 + \exp((x - 8.0409) / 0.4744))$ (where x is W, SWL, SWU, SW, S, y is elastic moduli), where the elastic modulus increases from 1.22 GPa in W specimen to 5.14 GPa in S specimen. The relationship between the peak strain and rock type can be described by a nonlinear relationship $y = 12.43 + 13129.2504 / (1 + \exp((x - 0.4954) / 0.6960))$ (where x is W, SWL, SWU, SW, S, y is peak strain), where the peak strain decreases from 21.74‰ in specimen W to 9.19‰ in SWL specimen then increases from 9.19‰ in SWL specimen to 15.16‰ in S specimen. And the relationship between the peak strength and rock types can be described by a nonlinear relationship $y = 77.9101 - 55.2834 / (1 + \exp((x - 4.2014) / 0.0605))$ (where x is W, SWL, SWU, SW, S, y is peak strength),

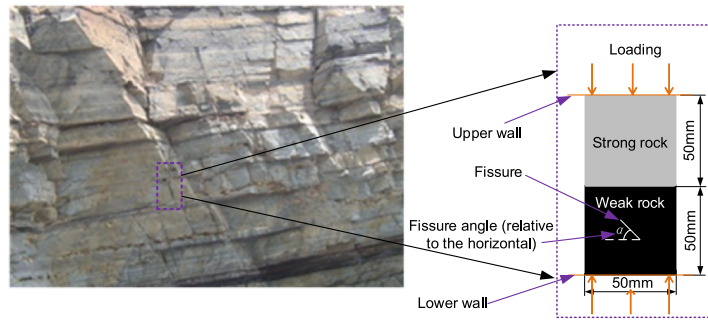


Fig. 5. Numerical simulation of double-layer composite rock specimens under uniaxial compression (fissure angle is relative to the horizontal).

where the peak strength decreases from 26.53 MPa in W to 16.61 MPa in SWL, then increases from 16.61 MPa in SWL to 77.91 MPa in S specimen.

Table 2 shows the failure characteristics of the W, SWL, SWU, SW and S specimens. Regardless of whether it is SWL, SWU or SW, the failure mainly occurs in the weaker part of the composite specimen. And compared with SWL, the failure of SWU and SW are more pervasively fractured. What is more, after the fracture-containing upper part of the SWU specimen is slightly damaged along the fissure, the main failure occurs in the lower part. However, the failure in SWL occurs only in the fracture-containing lower part. Overall, the mechanical properties of the SWL, SWU and SW specimens are intermediate between specimens W and S—as the presence of the fissure has weakened and softened the response.

Fig. 7 shows the stress–strain curves for SWL with different fissure angles and lengths. As can be seen from Fig. 7(a), peak strength increases with the fissure angle and the slope of the stress–strain response becomes stiffer. When the fissure angle is increased to 45° and 60°, the stress–strain curve appears steps-down post-peak. The peak strengths decrease with fissure length, and the stiffness diminishes, as shown in Fig. 7(b). When the fissure length is 4 mm, the stress–strain curves show a rapid decrease post-peak. The rest of the stress–strain curves have step-downs post-peak.

Fig. 8 shows the mechanical parameters of the SWL specimen containing a pre-existing fissure with different angles and lengths under uniaxial compression. The results show that the elastic moduli, peak strain and peak strength of the SWL specimens all increase with increasing fissure angles. The relationship between the elastic moduli and fissure angles can be described by a nonlinear relationship $y = 1.9656 - 0.4957 / (1 + \exp((x - 52.7301) / 12.3811))$ (where x is fissure angles, °, y is elastic moduli), where the elastic moduli increases from 1.490 GPa for a fissure at 0° to 1.953 GPa at 90°. The relationship between the peak strain and fissure angles can be described by a nonlinear relationship $y = 12.5495 - 2.7856 / (1 + \exp((x - 74.9932) / 0.2005))$ (where x is fissure angles, °, y is peak strain), where the peak strain increases from 10.417 % in the SWL sample with a fissure angle of 0° to 12.549 % at 90°. And the relationship between the peak strength and fissure angles can be described by a nonlinear relationship $y = 25.2199 - 9.4856 / (1 + \exp((x - 72.4) / 6.7142))$ (where x is fissure angles, °, y is peak strength), where the peak strength increases from 15.439 MPa at a fissure angle of 0° to 24.542 MPa at 90°.

Elastic moduli, peak strain and peak strength of the SWL specimens all decrease with increasing fissure lengths. The relationship between the elastic moduli and length can be described by a nonlinear relationship $y = 8.7792 - 5.4084 / (1 + \exp((x - 6.8462) / 3.6459))$ (where x is fissure length, mm, y is elastic moduli), where the elastic moduli decreases from 1.956 GPa for a fissure angle of 0° to 1.250 GPa at 90°. The relationship between the peak strain and fissure length can be described by a nonlinear relationship $y = 12.5495 - 2.7856 / (1 + \exp((x - 74.9932) / 0.2005))$ (where x is fissure length, mm, y is peak

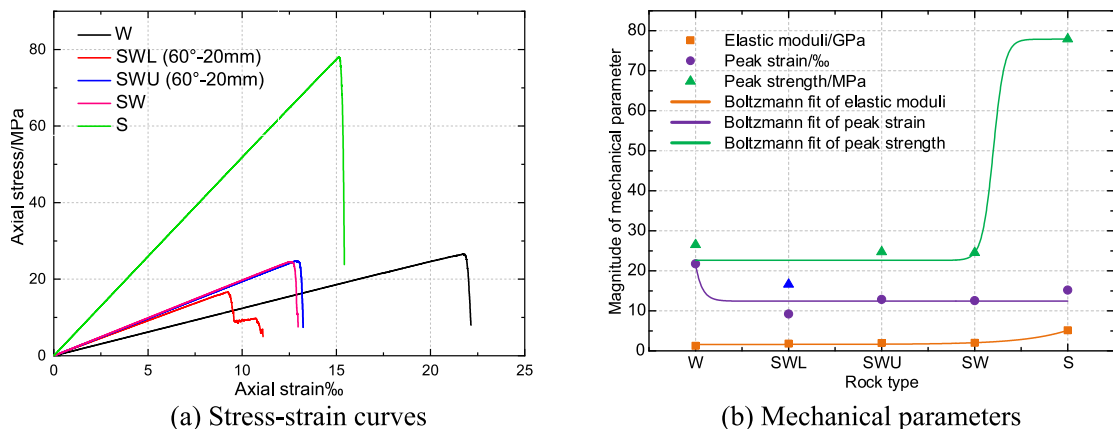
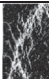


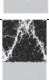



Fig. 6. Stress–strain curves and change in mechanical parameters for different layered specimen configurations.

Table 2
Mechanical parameters and failure characteristics of the five configurations of rock specimens.

Rock specimens	Peak strength/MPa	Peak strain/ 10^{-3}	Elastic moduli/GPa	Failure characteristics
W	26.53	21.74	1.22	
SWL	16.61	9.19	1.81	
SWU	24.74	12.82	1.93	
SW	24.54	12.55	1.97	
S	77.91	15.16	5.14	

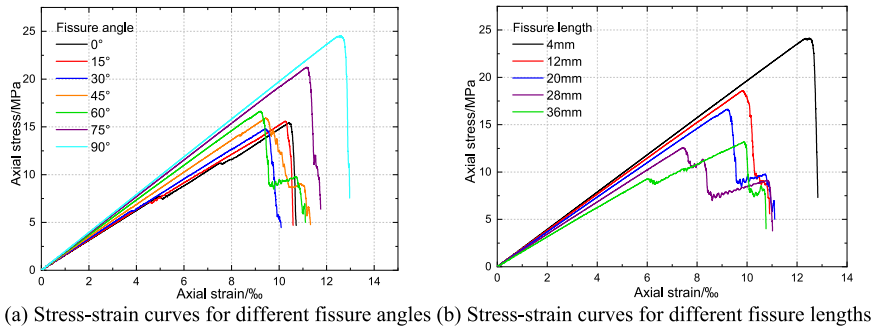


Fig. 7. Stress-strain curves of SWL specimens with different fissure angles and lengths.

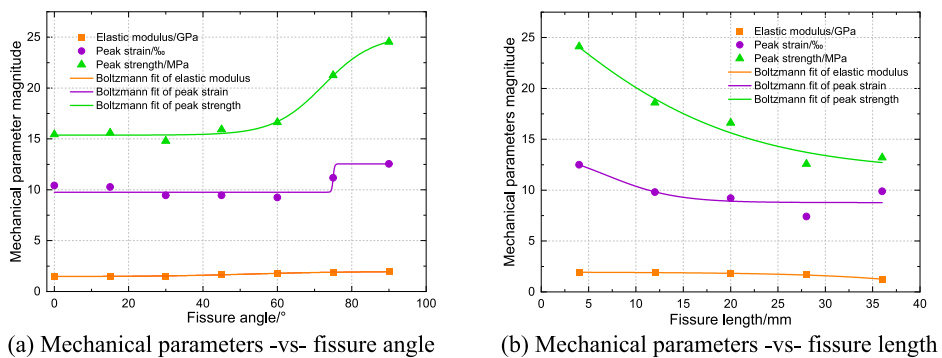


Fig. 8. Change in mechanical parameters for different fissure angles and lengths.

strain), where the peak strain decreases from 12.481 % for a fissure angle of 0° to 9.893 % at 90°. And the relationship between the peak strength and fissure length can be described by a linear relationship $y = 25.2199 - 9.4856 / (1 + \exp((x - 72.4) / 6.7142))$ (where x is fissure length, mm, y is peak strength), where the peak strength decreases from 24.136 MPa at a fissure angle of 0° to 13.209 MPa at 90°.

3.2. AE characteristics

Specimens W and SWL (fissure = 45°-20 mm, 60°-20 mm and 60°-36 mm), SWU, SW and S are selected to display their stress-strain curves, crack number, AE events and failure characteristics, as shown in Fig. 9. Regardless of the type of weak (W) or strong (S) samples, the AE events can be divided into three phases: quiescent phase, slow crack-generation phase, and rapid crack-growth phase. The W uniform specimens and SWU, SW and S all have a longer quiet period. There is a slow AE generation stage before the peak in the stress-strain curve and a rapid increase occurs immediately thereafter. In addition, the number of AE events generated during the second stress drop of the SWL specimen after the stress-strain peak is greater than that of the first. The number of AE events at peak strength in descending order is: specimens S > W > SWU(60°-20 mm) > SW > SWL(60°-20 mm) = SWL(60°-36 mm) > SWL(45°-20 mm).

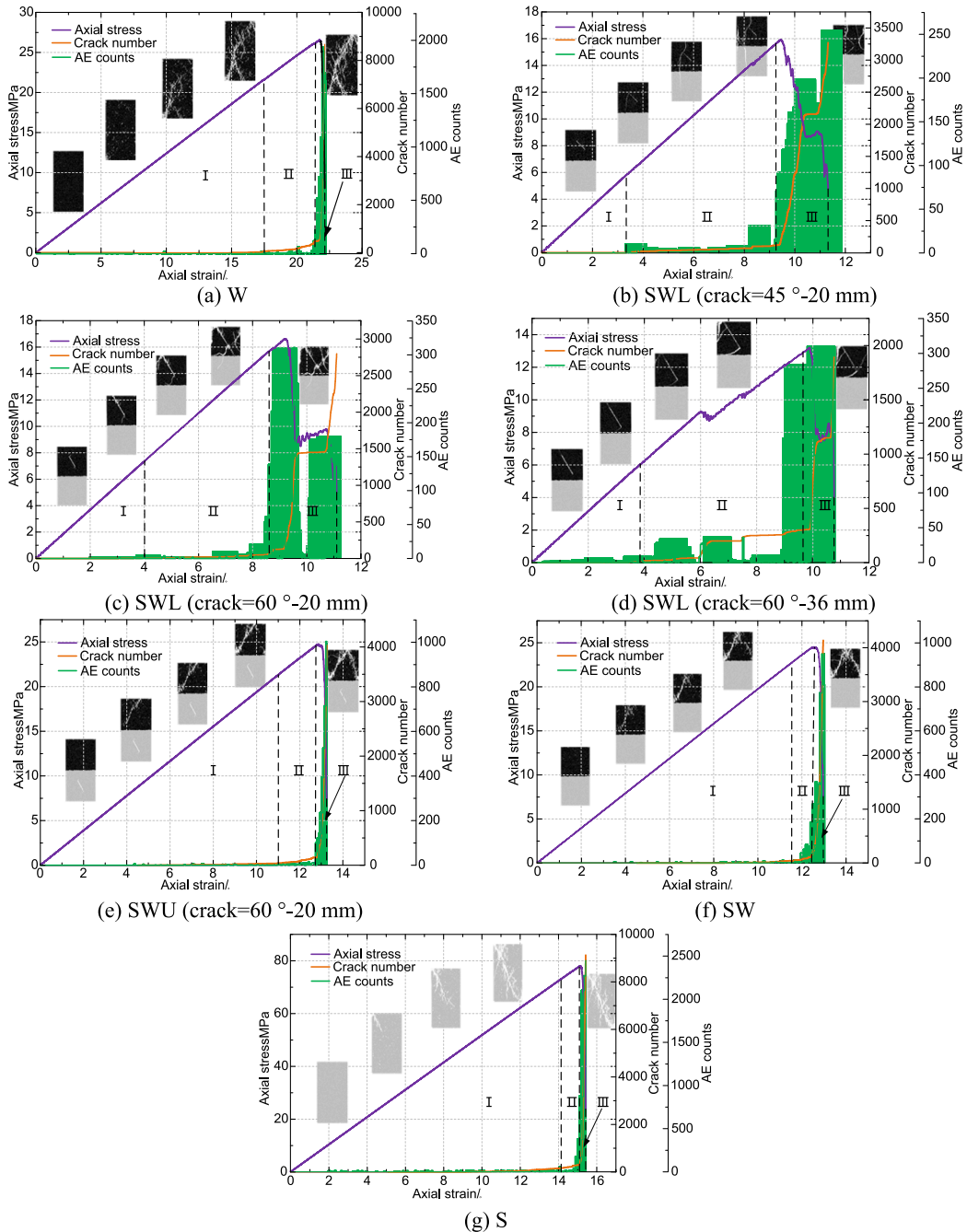


Fig. 9. Number of cracks, AE events and failure characteristics of W, SWL, SWU, SW and S specimens.

Apparent from Fig. 9(b) and (c) is that the maximum number of AE events increases from 248 to 311 when the fissure angle increases from 45° to 60° for the same fissure length. At the same fissure angle, as the length of the fissure increases from 20 mm to 36 mm, the maximum value of AE events is remains the same - although the strain developed at the maximum AE counts is different. The maximum AE count at 20 mm occurs at the first step post-peak, and the maximum at 36 mm occurs after the second stress-drop, as shown in Fig. 9(c) and (d).

The failure process of the specimens during uniaxial compression is shown in Fig. 9. From Fig. 9, regardless of the fissure length and angle, fracture in the SWL or SW specimens first occurs in the lower and weaker part of the composite specimens. The fracture of SWL occurs at the tip of the fissure first, and then expands into the remainder of the weak lower part. As the loading progresses, the fracture expands into the strong upper part. But as the fissure angle increases, the fracture in the strong upper part gradually decreases, as shown in Fig. 9(b), (c) and (d). The fracture of SW also occurs first at the two tips of the fissure, but instead of continuing to expand into the upper part, the lower part is partially ruptured, resulting in overall failure.

3.3. Failure characteristics

Table 3 shows the failure characteristics of the SWL specimens with different fissure angles. The main cracks mainly extend to the lower and weaker zone along both ends of the fissures. When the fissure angle is small, the damage to the lower rock in the composite specimen is relatively small but grows as the fissure angle increases. When the fissure angle is 30, 45 or 75°, the crack extends into the upper part of the composite specimen. When the fissure angle is 45°, the upper part of the composite specimen has the greatest damage, followed by 30°. At 75°, the damage in the least in the upper part compared to 30 and 45°. This is different from the composite specimen with a fissure in upper part. When the fissure angle in the upper stronger layer is 30, 45 and 75°, the main failure of the composite specimen still occurs in the lower part, as shown in Table 3 [40].

The influence of fissure lengths on the failure characteristics of the SWL specimens is listed in Table 4. The failure of the composite specimens with different fissure lengths mainly occurs in the lower weaker part. Only when the fissure length is 12 mm does the damage extends to the upper stronger region and becomes obvious. And regardless of the fissure lengths, the fractures are generated at both ends of the fissures, and the main fractures generated in the weaker lower part near the interface with the stronger upper part. Congruent with the SWL specimens, the fracture of the SWU specimens occurs in the part hosting the fissure. Only when the fissure is long enough does the upper part break, such as SWU specimen with a fissure length of 40 mm. This is different from the fracture of SWL specimens [40].

3.4. Rock burst tendency

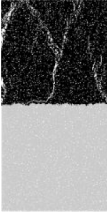
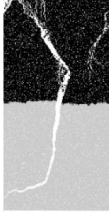
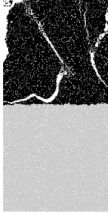
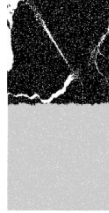
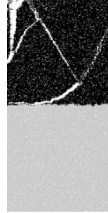





Rock bursting is a rapid and typically dangerous release of energy that may cause damage to adjacent structures and personnel [41–43]. Rock burst energy index, elastic energy index, dynamic failure time, uniaxial compressive strength and bending energy index are all used as the diagnostic indicators of rock burst tendency [44–47]. The rock burst energy index K_E is the ratio of the elastic deformation energy (A_s) accumulated before the peak strength to the elastic deformation energy (A_x) released post- peak, as shown in Eq. (4) and Fig. 10. $K_E > 1.5$ denotes a tendency to burst.

$$K_E = \frac{A_s}{A_x} \tag{4}$$

Table 3
Effect of fissure angles on the failure characteristics of the SWL specimens.

Fissure angles/°	0	15	30	45	60	75	90
Failed specimens (SWL)							
Failed specimens (SWU) ⁴⁰							

Table 4
Effect of fissure lengths on the failure characteristics of the SWL specimens.

Fissure lengths/mm	4	12	20	28	36
Failed specimens					
Fissure lengths/mm	5	15	25	30	40
Failed specimens (SWU) ⁴⁰					

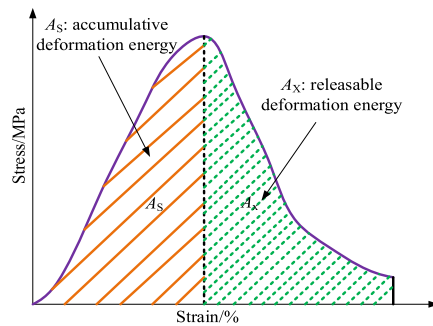


Fig. 10. Definition of various rock burst indicators, defining KE [44–46].

Fig. 11 shows the A_S , A_X , A and K_E of W, SWL, SWU, SW and S specimens. Fig. 11(b) shows the influence of fissure angles on rock burst energy index K_E . With an increase in fissure angles, K_E first decreases and then increases. The relationship between K_E and fissure angles can be described by a nonlinear expression $y = 9.1140 + (-455.3205/42.1386 * \sqrt{\pi/2}) * \exp(-2 * (x - 51.4573)/42.1386)^2$ (where x is fissure angles, $^\circ$, y is K_E). K_E at 90° is smaller than that at 0° . In addition, K_E is less than 1.5 and non-burst-prone when the fissure angles are 45° and 60° . That is to say, a fissure at 45° to 60° can effectively reduce the rock burst tendency of the SWL specimens.

Apparent from Fig. 11(d) is that K_E decreases to be non-burst-prone for intermediate lengths. The relationship between the K_E and length can be described by a nonlinear relationship $y = 43713.1463 + 43713.1181 * \sin(\pi * (x + 4814.6311)/3225.7010)$ (where x is fissure length, mm, y is K_E). Finally, from Fig. 11(f), only K_E of the SWL specimen is less than 1.5, and is non-burst-prone.

4. Discussion

Fissure angles, lengths and positions all exert an influence on the mechanical properties, microcrack evolution, AE events and rock burst tendency of layered composite rock masses. The purpose of this study is to analyze the influence of the positions, lengths and angles of fissures in composite materials on the mechanical behavior and failure mechanisms with reference stability evaluation and disaster mitigation.

(1) For W, SWL, SWU (60° -20 mm), SW and S specimens - strength is always bracketed between the weak (W) and strong (S) specimens. Failure mainly occurs in the weak layer of the composites, as noted previously [40]. But the difference is that when the fissure length in the SWL specimen is 20 mm, the angle is 30° , 45° , 75° and the length is 12 mm, and the angle is 60° , the fracture will penetrate the strong layer (as shown in Tables 3 and 4). Table 5 shows the failure characteristics of SWU with different fissure length at

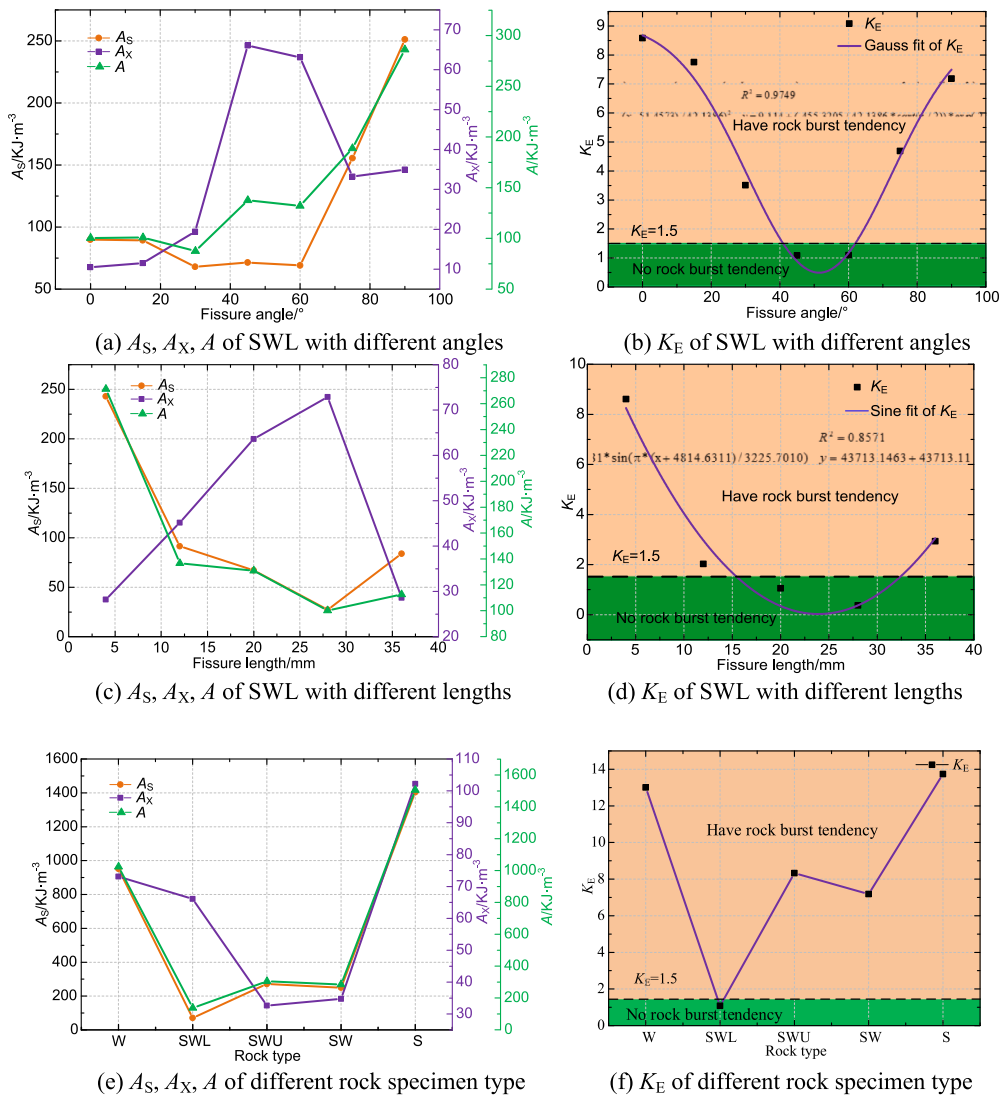


Fig. 11. A_S, A_X, A and K_E of W, SWL, SWU, SW and S specimens.

Table 5
Failure characteristics of SWU specimens with different fissure lengths when the fissure angle is 60° .

Fissure lengths/mm	4	12	20	28	36
Failed specimens (SWU, 60°)					

an angle of 60° , which is different from that in the physical rock mechanics test [40]. As can be seen from Tables 3, 4 and 5, the failure mechanism of the double-layer composite rock specimens is not only caused by the crack propagation in the weak layer, but also results in failure of entire specimen when the length of the fissure in the strong layer is large enough. This is different from prior observations

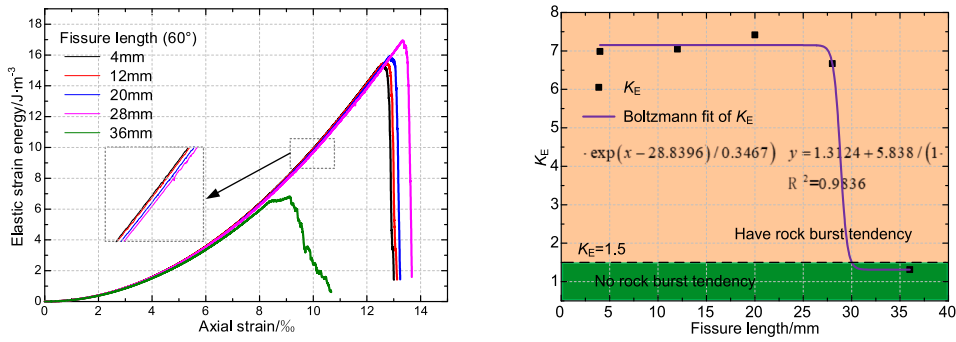


Fig. 12. Elastic strain energy and K_E of SWU with different lengths when fissure angle is 60°.

[11] that showed that the failure mechanism of the specimen is mainly caused by crack propagation in the weaker layer.

(2) The rock burst energy index K_E of specimens SW, SWL and SWU is less than that of W and S. The numerical simulation results in this paper are different from the results obtained by Zuo et al. [48–50] through physical rock mechanics experiments. Zuo et al.'s [48–50] observations were that “compared with the weak single specimen, the rock burst energy index of the composite specimen is increased, and the layer composite specimen improves the rock burst tendency of the weak rock.” However, we observe that the rock burst tendency of the layered composite specimen is less than that of the weak homogeneous (W) specimen. The main reason may be the heterogeneity of the weak and strong materials and the influence of the weak/strong interface used in the laboratory.

When the fissure angle is 60° and the length 20 mm, the rock burst energy index K_E of the SWL specimen is less than 1.5, thus it has no rock burst tendency. It can also be seen from Fig. 11 that the rock burst energy index K_E first decreases and then increases with increases in the fissure angles or lengths. The rock burst energy index K_E for SWL is less than 1.5 when the fissure angles are 45 and 60° and the lengths are 20 and 28 mm. In order to compare whether cutting a fissure in weak or strong layers can effectively reduce the rock burst tendency, SWU specimens with different fissure lengths at an angle of 60° are analyzed. The curves of elastic strain energy versus strain and also rock burst energy index K_E versus length are shown in Fig. 12. It can be seen from Fig. 12(a) that when the fissure angle of SWU is 60°, the elastic strain energy first increases and then decreases during the entire experiment. And the elastic strain energy at the peak strength first increases and then decreases with the increase of fissure lengths. When the length increases from 28 mm to 36 mm, the elastic strain energy decreases rapidly, and is smaller than for other lengths. As can be seen from Fig. 12(b), when the fissure angle is 60°, the rock burst energy index K_E first increases and then decreases with the increase of length. The rock burst energy index of the SWL geometry is opposite to the change in length. Only when the fissure length in SWU is long enough, is the rock burst energy index K_E less than 1.5, and there is no rock burst tendency. Based on the above analysis, fissures cut in the weak rock or in the strong rock will both reduce the rock burst tendency. But regardless of whether it is in weak or strong rock, it is necessary to control the fissure angles and lengths. Compared with cutting fissures in the strong rock, the angles of the fissures in the weak rock are more flexible, and the lengths of the fissures are relatively short.

(3) However, it should be pointed out that at present, the rock burst energy index, elastic energy index, dynamic failure time, uniaxial compressive strength and bending energy index are used as the classification indexes for rock burst tendency. In this paper, the rock burst energy index K_E is solely used, although other parameters may be relevant.

5. Conclusions

We examine the influence of the positions, inclination angles (relative to the horizontal) and lengths of pre-existing fissures on the mechanical properties of layered composite specimens using granular mechanics models—inclusive of rock burst energy index K_E . These observations are used to index failure and stability related to catastrophic failure. The primary conclusions are as follows:

(1) The peak strengths and elastic moduli of all composite specimens (SW, SWL, SWU) are intermediate between those of the weak (W) and strong (S) rock specimens. The elastic moduli and peak strengths both increase with an increase in the inclination of the fissure angles and both decrease with an increase in the fissure lengths.

(2) The number of AE events, micro cracks and their failure characteristics in all samples clearly correspond to the stress–strain curves. The number of AE events at peak strength, in descending order are: S specimen > W specimen > SWU specimen (60°-20 mm) > SW specimen > SWL specimen (60°-20 mm) = SWL specimen (60°-36 mm) > SWL specimen (45°-20 mm).

(3) As the fissure angle in the weaker (lower, SWL) material increases from 0° to 75° (relative to the horizontal), damage in the surrounding matrix becomes increasingly more severe—except when the fissure is aligned in the loading direction at 90°. At angles of 30, 45, 75°, the crack will extend into the stronger layer, with the most damage when at 45°. Conversely, when the fissure is in the stronger (upper, SWU) material, the principal damage occurs in the underlying weaker layer rather than proximal to the fracture. Only when the fissure is long enough will the hosting strong material fracture.

(4) The burst tendency for the composite specimens is effectively reduced by a fissure within either the weak (lower, SWL) or strong (upper, SWU) layers—but only for a range of fissure inclination angles and lengths. Therefore, in engineering practice, it is recommended to cut fissures in the lower (weaker) rock layer. Compared to cutting fissures in the upper (stronger) rock, the angles of the

fissures in the lower (weaker) rock are more flexible. And the lengths of fissures are relatively short, the workload is reduced, and the cost is also reduced.

The evaluation of rock burst tendency is based exclusively on the rock burst energy index K_E , neglecting other parameters as elastic energy index (W_{ET}), dynamic failure time (D_T), and uniaxial compressive strength (UCS). Further studies may similarly examine the importance of these various indices.

CRedit authorship contribution statement

Qing Ma: Formal analysis, Writing – original draft. **Xiaoli Liu:** Funding acquisition, Writing – review & editing. **Yunliang Tan:** Funding acquisition. **Derek Elsworth:** Conceptualization, Investigation, Writing – review & editing. **Junlong Shang:** Data curation, Validation. **Danqing Song:** Investigation. **Xuesheng Liu:** Funding acquisition. **Fayuan Yan:** .

Declaration of Competing Interest

The authors declare that they have no known competing financial interests or personal relationships that could have appeared to influence the work reported in this paper.

Data availability

Data will be made available on request.

Acknowledgments

This study was financially supported by the National Natural Science Foundation of China (Grant Nos. 51874190, 52079068, 41941019, 52090081, 52074168), the Climbling Project of Taishan Scholar in Shandong Province (Grant No. tspd20210313), and the State Key Laboratory of Hydroscience and Engineering, China (Grant No. 2021-KY-04). DE acknowledges support from the G. Albert Shoemaker endowment.

References

- [1] Shang JL, Hencher SR, West LJ. Tensile strength of geological discontinuities including incipient bedding, rock joints and mineral veins. *Rock Mech Rock Eng* 2016;49:4213–25. <https://doi.org/10.1007/s00603-016-1041-x>.
- [2] Xu DP, Feng XT, Chen DF, Zhang CQ, Fan QX. Constitutive representation and damage degree index for the layered rock mass excavation response in underground openings. *Tunn Undergr Sp Tech* 2017;64:133–45. <https://doi.org/10.1016/j.tust.2017.01.016>.
- [3] Zhao ZH, Liu H, Gao XJ, Feng YH. Meso-macro damage deterioration of weakly cemented red sandstone under the coupling effect of high-humidity and uniaxial loading. *Eng Fail Anal* 2023;143:106911. <https://doi.org/10.1016/j.engfailanal.2022.106911>.
- [4] Zhang T, Chen QZ, Zhang JZ, Zhou XP. Influences of mechanical contrast on failure characteristics of layered composite rocks under true-triaxial stresses. *Rock Mech Rock Eng* 2023. <https://doi.org/10.1007/s00603-023-03341-z>.
- [5] Shang JL, West LJ, Hencher CR, Zhao Z. Geological discontinuity persistence: implications and quantification. *Eng Geol* 2018;241:41–54. <https://doi.org/10.1016/j.enggeo.2018.05.010>.
- [6] Shang JL. Rupture of veined granite in polyaxial compression: insights from three dimensional discrete element method modelling. *J Geophys Res: Solid Earth* 2020;125(2):1–25. <https://doi.org/10.1029/2019JB019052>.
- [7] Zhu JB, Li H, Deng JH. A one-dimensional elastoplastic model for capturing the nonlinear shear behaviour of joints with triangular asperities based on direct shear tests. *Rock Mech Rock Eng* 2018;52(6):1671–87. <https://doi.org/10.1007/s00603-018-1674-z>.
- [8] Liu XL, Han GF, Wang EZ, Wang SJ, Nawnit K. Multiscale hierarchical analysis of rock mass and prediction of its mechanical and hydraulic properties. *J Rock Mech Geotech Eng* 2018;10(4):694–702. <https://doi.org/10.1016/j.jrmge.2018.04.003>.
- [9] Stead D, Wolter A. A critical review of rock slope failure mechanisms: the importance of structural geology. *J Struct Geol* 2015;74:1–23. <https://doi.org/10.1016/j.jsg.2015.02.002>.
- [10] Zhang JZ, Zhou XP. Fracture process zone (FPZ) in quasi-brittle materials: Review and new insights from flawed granite subjected to uniaxial stress. *Eng Fract Mech* 2022;274:108795. <https://doi.org/10.1016/j.engfracmech.2022.108795>.
- [11] Lin QB, Cao P, Wen GP, Meng JJ, Cao RH, Zhao ZY. Crack coalescence in rock-like specimens with two dissimilar layers and pre-existing double parallel joints under uniaxial compression. *Int J Rock Mech Min Sci* 2021;139:104621. <https://doi.org/10.1016/j.ijrmm.2021.104621>.
- [12] Zhou XP, Zhang JZ, Yang SQ, Berto F. Compression-induced crack initiation and growth in flawed rocks: a review[J]. *Fatigue Fract Eng M* 2021;44(7):1681–707. <https://doi.org/10.1111/ffe.13477>.
- [13] Liu XL, Wang SJ, Wang EZ, Wang JX, Hu B. Evolutionary rules of flaws in rock subjected to uniaxial compression and rock strength. *Chinese J Rock Mech Eng* 2008;27(6):1195–201. In Chinese.
- [14] Niu Y, Zhou XP, Berto F. Evaluation of fracture mode classification in flawed red sandstone under uniaxial compression. *Theor Appl Fract Mech* 2020;107:102528. <https://doi.org/10.1016/j.tafmec.2020.102528>.
- [15] Li XB, Feng F, Li DY. Numerical simulation of rock failure under static and dynamic loading by splitting test of circular ring. *Eng Fract Mech* 2018;188:184–201. <https://doi.org/10.1016/j.engfracmech.2017.08.022>.
- [16] Zhou XP, Zhang JZ. Damage progression and acoustic emission in brittle failure of granite and sandstone. *Int J Rock Mech Min Sci* 2021;143(1):104789. <https://doi.org/10.1016/j.ijrmm.2021.104789>.
- [17] Wong LNY, Guo TY, Wu ZJ, Xiao XY. How do thermally induced microcracks alter microcracking mechanisms in Hong Kong granite? *Eng Geol* 2021;292:106268. <https://doi.org/10.1016/j.enggeo.2021.106268>.
- [18] Reyes O, Einstein HH. Failure mechanisms of fractured rock—a fracture coalescence model. In: *7th ISRM Congress 1991*;vol. 8.
- [19] Yang SQ, Huang YH, Tian WL, Zhu JB. An experimental investigation on strength, deformation and crack evolution behavior of sandstone containing two oval flaws under uniaxial compression. *Eng Geol* 2017;217:35–48. <https://doi.org/10.1016/j.enggeo.2016.12.004>.
- [20] Bobet A, Einstein HH. Fracture coalescence in rock-type materials under uniaxial and biaxial compression. *Int J Rock Mech Min Sci* 1998;35(7):863–88. [https://doi.org/10.1016/S0148-9062\(98\)00005-9](https://doi.org/10.1016/S0148-9062(98)00005-9).

- [21] Zhou XP, Zhang JZ, Qian QH, Niu. Experimental investigation of progressive cracking processes in granite under uniaxial loading using digital imaging and AE techniques. *J Struct Geol* 2019;126:129–45. <https://doi.org/10.1016/j.jsg.2019.06.003>.
- [22] Zhang JZ, Zhou XP. AE event rate characteristics of flawed granite: from damage stress to ultimate failure. *Geophys J Int* 2020;222(2):795–814. <https://doi.org/10.1093/gji/ggaa207>.
- [23] Zhang JZ, Zhou XP, Du YH. Cracking behaviors and acoustic emission characteristics in brittle failure of flawed sandstone: a true triaxial experiment investigation. *Rock Mech Rock Eng* 2022;204:1–16. <https://doi.org/10.1007/s00603-022-03087-0>.
- [24] Shen BT, Stephansson O, Einstein HH, Ghahreman B. Coalescence of fractures under shear stresses in experiments. *J Geophys Res: Solid Earth* 1995;100(B4):5975–90. <https://doi.org/10.1029/95jb00040>.
- [25] Wang YT, Zhou XP, Xu X. Numerical simulation of propagation and coalescence of flaws in rock materials under compressive loads using the extended non-ordinary state-based peridynamics. *Eng Fract Mech* 2016;163:248–73. <https://doi.org/10.1016/j.engfracmech.2016.06.013>.
- [26] Ma Q, Tan YL, Liu XS, Gu QH, Li XB. Effect of coal thicknesses on energy evolution characteristics of roof rock-coal-floor rock sandwich composite structure and its damage constitutive model. *Compos Part B-Eng* 2020;198:108086. <https://doi.org/10.1016/j.compositesb.2020.108086>.
- [27] Tan YL, Ma Q, Liu XS, Zhao ZH, Zhao MX, Liang L. Failure prediction from crack evolution and acoustic emission characteristics of coal-rock sandwich composite samples under uniaxial compression. *B Eng Geol Environ* 2022;81(5):1–15. <https://doi.org/10.1007/s10064-022-02705-z>.
- [28] Lockner D. The role of acoustic emission in the study of rock fracture. *J Rock Mech Min Sci Geomech Abstr* 1993;30(7):883–99. [https://doi.org/10.1016/0148-9062\(93\)90041-B](https://doi.org/10.1016/0148-9062(93)90041-B).
- [29] Zhang Q, Zhang XP, Yang SQ. Numerical study of fracture failure nature around the circular and horseshoe openings using the bonded-particle model. *Geophys J Int* 2023;232:725–37. <https://doi.org/10.1093/gji/ggac360>.
- [30] Zhao TB, Guo WY, Lu CP, Zhao GM. Failure characteristics of combined coal-rock with different interfacial angles. *Geomech Eng* 2016;11(3):345–59. <https://doi.org/10.12989/gae.2016.11.3.345>.
- [31] Ma Q, Tan YL, Liu XS, Zhao ZH, Fan DY. Mechanical and energy characteristics of coal-rock composite sample with different height ratios: a numerical study based on particle flow code. *Environ Earth Sci* 2021;80(8):309. <https://doi.org/10.1007/s12665-021-09453-5>.
- [32] Zhang JZ, Zhou XP. Forecasting catastrophic rupture in brittle rocks using precursory AE time series. *J Geophys Res-Sol EA* 2020;125(8):1–20. <https://doi.org/10.1029/2019JB019276>.
- [35] Tien YM, Kuo MC, Juang CH. An experimental investigation of the failure mechanism of simulated transversely isotropic rocks. *Int J Rock Mech Min Sci* 2006;43(8):1163–81. <https://doi.org/10.1016/j.ijrmms.2006.03.011>.
- [36] Wang YT, Zhou XP, Wang Y, Shou YD. A 3-D conjugated bond-pair-based peridynamic formulation for initiation and propagation of cracks in brittle solids. *Int J Solids Struct* 2018;134:89–115. <https://doi.org/10.1016/j.ijsolstr.2017.10.022>.
- [37] Zhang T, Zhou XP, Qian QH. Drucker-Prager plasticity model in the framework of OSB-PD theory with shear deformation. *Eng Comput-Germany* 2023;39:1395–414. <https://doi.org/10.1007/s00366-021-01527-z>.
- [38] Potyondy DO, Cundall PA. A bonded-particle model for rock. *Int J Rock Mech Min Sci* 2004;41(8):1329–64. <https://doi.org/10.1016/j.ijrmms.2004.09.011>.
- [39] Itasca Consulting Group. PFC2D (particle flow code in 2 dimensions) Fish in PFC2D. Minneapolis, MN: Itasca Consulting Group; 2008.
- [40] Liu JW, Wu N, Si GY, Zhao MX. Experimental study on mechanical properties and failure behaviour of the pre-cracked coal-rock combination. *B Eng Geol Environ* 2020;80:2307–21. <https://doi.org/10.1007/s10064-020-02049-6>.
- [41] Kaiser PK, Cai M. Design of rock support system under rockburst condition. *J Rock Mech Geotech Eng* 2012;4(3):215–27.
- [42] Feng XT, Zhang CQ, Qiu SL, Zhou H, Jiang Q, Li SJ. Dynamic design method for deep hard rock tunnels and its application. *J Rock Mech Geotech Eng* 2016;8:443–61. <https://doi.org/10.1016/j.jrmge.2016.01.004>.
- [43] Sun H, Liu XL, Zhu JB. Correlation fractal characterization of stress and acoustic emission during coal and rock failure under multilevel dynamic loadings. *Int J Rock Mech Min Sci* 2019;117:1–10. <https://doi.org/10.1016/j.ijrmms.2019.03.002>.
- [44] GB/T 25217.2-2010. Classification and Laboratory Test Method On Bursting Liability Of Coal, Beijing: Standards Press of China, 2010.
- [45] Li CC. Principles and methods of rock support for rockburst control. *J Rock Mech Geotech* 2021;13(1):14. <https://doi.org/10.1016/j.jrmge.2020.11.001>.
- [46] Cai Wu, Dou L, Si G, Cao A, He J, Liu S. A principal component analysis/fuzzy comprehensive evaluation model for coal burst liability assessment. *Int J Rock Mech Min Sci* 2016;81:62–9.
- [47] Zhao ZH, Tan YL, Chen SJ, Ma Q, Gao XJ. Theoretical analyses of stress field in surrounding rocks of weakly consolidated tunnel in a high-humidity deep environment. *Int J Rock Mech Min Sci* 2019;122:104064. <https://doi.org/10.1016/j.ijrmms.2019.104064>.
- [48] Zuo JP, Chen Y, Cui F. Investigation on mechanical properties and rock burst tendency of different coal-rock combined bodies. *J China Univ Min Tech* 2018;47(1):81–7. <https://doi.org/10.13247/j.cnki.jcumt.000795>.
- [49] Zuo JP, Chen Y, Song HQ. Study progress of failure behaviors and nonlinear model of deep coal-rock combined body. *J Central South Uni Sci Tech* 2021;52(8):2510–21. <https://doi.org/10.11817/j.issn.1672-7207.2021.08.002>.
- [50] Song HQ, Zuo JP, Liu HY, Zuo SH. The strength characteristics and progressive failure mechanism of soft rock-coal combination samples with consideration given to interface effects. *Int J Rock Mech Min Sci* 2021;138:104593. <https://doi.org/10.1016/j.ijrmms.2020.104593>.